



Technical Note

MR Imaging and Electrophysiological Features of Doxorubicin-Induced Fibrosis: Protocol Development in a Small Preclinical Pig Study with Histological Validation [†]

Peter Lin ¹, Terenz Escartin ^{1,2}, Melissa Larsen ², Matthew Ng ², Mengyuan Li ³, Jennifer Barry ², Idan Roifman ⁴ and Mihaela Pop ^{2,*}

¹ Department of Medical Biophysics, University of Toronto, 101 College Street, Toronto, ON M5G 1L7, Canada

² Sunnybrook Research Institute, 2075 Bayview Avenue, Toronto, ON M4N 3M5, Canada

³ Institute of Biomedical Engineering, University of Toronto, 164 College Street, Toronto, ON M5S 3G9, Canada

⁴ Sunnybrook Health Sciences Centre, Department of Cardiology, 2075 Bayview Avenue, Toronto, ON M4N 3M5, Canada

* Correspondence: mihaela.pop@utoronto.ca

[†] This paper is (in part) an extended version of a conference proceeding paper published by Statistical Atlases and Computational Models of the Heart (STACOM) workshop, held in Strasbourg, France, 2021.

Abstract: A critical chemotherapeutic complication is cardiotoxicity, often leading, in time, to heart failure. In this work, we developed a novel animal protocol using magnetic resonance (MR) imaging and electrophysiology (EP) tests, designed to detect subtle structural and functional changes associated with myocardial damage in sub-chronic phases post-chemotherapy. A weekly dose of doxorubicin (DOX) was injected in four juvenile swine throughout a four-week plan, using an intravenous approach that mimics the treatment in cancer patients. We performed cardiac MR imaging as follows: in all four pigs pre-DOX; at 1 and 5 weeks post-DOX in a group of two pigs; and, at 1 and 9 weeks post-DOX in the other two pigs, using Cine imaging to assess ejection fraction (EF) and late gadolinium enhancement to quantify collagen density in the left ventricle. Additionally, X-ray-guided voltage mapping and arrhythmia tests were conducted in the group at 9 weeks post-DOX and in a healthy pig. Tissue samples were collected for histology. The results showed that EF decreased from ~46% pre-DOX to ~34% within the first 9 weeks post-DOX. This decline in LV function was explained by a gradual increase in collagen density, especially noticeable at week 9 post-DOX as derived from MRI analysis. Furthermore, ventricular fibrillation was induced via rapid pacing at 9 weeks post-DOX, most likely caused by fibrotic patches identified in voltage maps, as confirmed by MRI and collagen-sensitive histological stains. Overall, our novel preclinical protocol was able to reveal key signs of potentially-irreversible tissue changes, along with electrical remodeling and arrhythmia risk in the early months following DOX therapy. Future work will include more datasets to statistically power the study, and will use the protocol to test cardioprotective strategies.

Keywords: cardiotoxicity; MRI; fibrosis; chemotherapy; doxorubicin; voltage mapping; arrhythmia



Citation: Lin, P.; Escartin, T.; Larsen, M.; Ng, M.; Li, M.; Barry, J.; Roifman, I.; Pop, M. MR Imaging and Electrophysiological Features of Doxorubicin-Induced Fibrosis: Protocol Development in a Small Preclinical Pig Study with Histological Validation. *Appl. Sci.* **2022**, *12*, 11620. <https://doi.org/10.3390/app122211620>

Academic Editor: Qi-Huang Zheng

Received: 3 October 2022

Accepted: 13 November 2022

Published: 16 November 2022

Publisher's Note: MDPI stays neutral with regard to jurisdictional claims in published maps and institutional affiliations.



Copyright: © 2022 by the authors. Licensee MDPI, Basel, Switzerland. This article is an open access article distributed under the terms and conditions of the Creative Commons Attribution (CC BY) license (<https://creativecommons.org/licenses/by/4.0/>).

1. Introduction

Clinical motivation: Cardio-oncology is an emerging multi-disciplinary field that investigates the onset and progression of myocardial injury induced in cancer patients by chemo-therapeutic or molecular agents, as well as radiation therapy [1]. Among the FDA-approved anthracyclines, doxorubicin (DOX) hydrochloride is one of the most effective chemotherapeutic drugs prescribed in the treatment of breast cancer [2]. DOX has been also used in the treatment of bladder cancer, lymphoma (Hodgkin and non-Hodgkin), Kaposi's sarcoma, and acute lymphocytic leukemia, as well as metastatic cases (e.g., gastric cancer, ovarian cancer, neuroblastoma). However, despite the therapeutic benefit offered by DOX, preclinical and clinical studies have increasingly reported progressive heart dysfunction

as a critical adverse consequence of DOX-based treatments [3,4]. Furthermore, pharmacological studies showed that while DOX therapy induces cell death and cancer regression, it also triggers a problematic mechanism associated with cardiotoxicity based on a cascade of events that includes reactive oxidative stress [5] and modulation of mitochondrial function [6].

While the mechanism of cardiotoxicity remains somewhat controversial, it has been demonstrated that the cardiotoxic effects in myocytes and endothelial cells are primarily dose-dependent, leading to long-term irreversible damage of remodeled tissue, abnormal excitation–contraction coupling, and inefficient blood pumping. These major ventricular function impairments have been attributed to a gradual deposition of reactive collagenous fibrosis, causing cardiovascular complications such as cardiomyopathy or congestive heart failure and leading to collateral mortality in cancer survivors [1,2]. For decades, clinical studies have documented such cardiotoxic effects induced by anthracyclines only in late chronic stages, that is, after cardiomyopathy, heart failure and lethal events had occurred. Some recent investigations have focused on studying biological and physiological consequences in acute and subacute phases following chemotherapy, suggesting that both apoptosis and edema (i.e., fluid accumulation) occur within a time window of days and weeks post-DOX. In contrast, the irreversible myocardial damage, which is primarily represented by a gradual deposition of reactive fibrosis due to increased deposition of extracellular matrix (ECM), is believed to occur in sub-chronic and later phases following chemotherapy [1–4]. Moreover, only a limited number of clinical studies have related arrhythmia to cardiotoxicity in cancer survivors as a suspected causation of abnormal heart rhythms post-chemotherapy, despite the fact that these aberrant rhythms can degenerate into potentially lethal events such ventricular fibrillation [7].

1.1. Image-Based Methods to Evaluate Chemotherapy-Induced Cardiotoxic Effects

Clinical protocols and diagnostic methods routinely use echocardiographic imaging and have reasonable sensitivity and specificity in comprehensively monitoring and detecting DOX-mediated functional changes [8], while biopsy sampling is invasive and sparse, often missing structurally damaged tissue. Thus, the irreversible injury evolves undetected, worsening in time and leading, within months and years, to cardiomyopathy, and eventually to heart failure. Therefore, there has been a critical need to develop more accurate methods to detect earlier the cardiotoxic effects in sub-chronic phases following DOX-based therapies. With this respect, MR imaging offers excellent tissue contrast. For example, one group recently utilized MRI to assess cardiotoxicity in breast cancer survivors, showing that most patients had significantly different values of ejection fraction and global strain post-DOX compared to the baseline, and some presented evidence of diffuse fibrosis [9]. While 2D Cine and Late Gadolinium Enhancement methods are able to characterize post-DOX functional and structural changes [9], these scans typically use protocols with large slice thickness (~8–10 mm), similarly to those in acute or chronic infarct scars [10]. Current T1 and T2 mapping methods can differentiate, overall, the injured myocardium post-chemotherapy [11]; however, these low-resolution images (voxel size $2 \times 2 \times 10 \text{ mm}^3$) might miss subtle structural alterations. Thus, advanced methods using high-resolution 3D imaging should be adapted for imaging protocols of post-DOX evaluation.

1.2. Role of Pre-Clinical Animal Models of Cardiotoxicity

Animal models of cardiotoxicity represent a reasonable alternative to clinical investigations, allowing us to perform detailed and controlled studies that can address unanswered clinical questions. For example, image-based longitudinal studies in animals can reveal new biomarkers of adverse myocardial remodeling at different time points following DOX therapy, improving our mechanistic understanding regarding reversible vs. irreversible effects. Such models can be used to test more effective cardioprotective strategies prior to implementation in clinical trials. Furthermore, compared to sparse in vivo biopsy sam-

pling, animal models hold the great advantage of allowing us to study the entire heart after explantation for the purpose of histopathological assessment.

With respect to this, a large body of literature has reported the development of pre-clinical models of chemotherapy-induced cardiotoxicity. Many chronic models using small animals (e.g., mice [12], rabbits [13], mini-pigs [14]), have clearly demonstrated that the severity of structural myocardial remodeling is dependent on the cumulative dose of the chemotherapeutic drug, leading to mechanical dysfunction with poor ejection fraction and progressive heart failure. Unfortunately, small animal models are less relevant to the clinical translation of diagnostic imaging methods. Thus, more recently, one research group developed a swine model of cardiotoxicity and used MR imaging to demonstrate that the prolongation of T2 parameter (indicating edema) is reversible in early stages post-DOX, and that the LV function declines gradually within the first few months post-DOX [15]. However, in this study, DOX was administered intracoronary through a catheter, an invasive procedure which does not mimic the chemotherapeutic plan in patients. Therefore, alternative delivery methods, such as the intravenous injection of doxorubicin (as done in patients), might be more realistic to study cardiotoxicity in large animal models.

The specific aims of our work here are: (1) to develop a translational swine model to study DOX-induced cardiotoxicity, precisely mimicking the intravenous delivery of doxorubicin in cancer patients; and (2) to establish subtle quantitative MR imaging features and electrophysiological characteristics of DOX-induced cardiotoxic effects in the sub-chronic phases post-DOX (i.e., weeks and a couple of months after the DOX treatment was ceased). Specifically, in this preclinical work, we propose an MR imaging protocol that allows us to monitor, post-DOX, the temporal evolution of the left ventricular function (i.e., via Cinematic methods) and of the structural alterations (i.e., using high-resolution 3D contrast-enhanced MR to detect deposition of collagenous fibrosis), along with histological validation. In addition, our novel experimental protocol includes a complex X-ray-guided electrophysiological study to evaluate endocardial bipolar voltage maps and arrhythmia inducibility following the completion of DOX treatment.

2. Methods

All preclinical animal experiments were approved by the research ethics board of the Animal Care Committee at our Sunnybrook Research Institute (Toronto), and the DOX-related procedures were performed while ensuring all biohazard safety requirements.

The design of the experimental animal study to evaluate DOX-induced cardiotoxicity included the following: DOX treatment delivered weekly via intravenous injection; functional and structural MRI imaging (pre-DOX and post-DOX delivery) and associated image analysis; X-ray guided electrophysiology studies (voltage mapping and arrhythmia inducibility); and, lastly, histological staining of select myocardial tissue samples. The associated pipeline of our research protocol is illustrated in Figure 1, where each component is described in more detail below.

2.1. Development of a Preclinical Large Animal Model to Study DOX-Induced Cardiotoxicity

In this work, we used $n = 4$ juvenile healthy Yorkshire swine, weighing 20–25 kg prior to the commencement of DOX injections. Note that an additional healthy swine was used as control for the electrophysiology studies and histological validation. The dosage of doxorubicin (i.e., 1 mg/kg) was given based on the pig's weight, as per the typical chemotherapeutic doses. For each delivery, DOX was diluted into a 100 mL bag of saline and administered intravenously (i.v.) either into the ear or using a vascular access port (VAP) designed for large animals. The DOX solution was slowly injected over a 20–30 min period. The four pigs receiving DOX treatment were split into 2 groups: (i) Group 1 (pig #1 and pig #2, respectively), sacrificed at 5 weeks post-DOX; and (ii) Group 2 (pig #3 and pig #4, respectively), sacrificed at 9 weeks post-DOX. This grouping was carried out to enable the validation of longitudinal observations at two time points vs. histology.

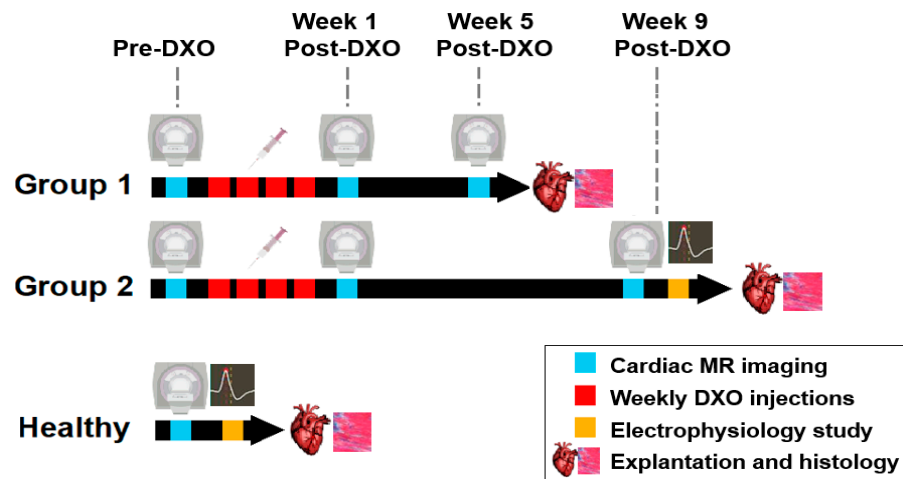


Figure 1. Pipeline of the experimental study to evaluate DOX cardiotoxicity pre- and post-treatment, as indicated by the arrows (the arrowheads point to the end of longitudinal studies).

2.2. *In Vivo* MR Imaging Protocol and Associated Analysis

MR imaging studies were conducted on a 3T whole body scanner (MR 750, General Electric Healthcare, Waukesha, WI, USA). Prior to imaging (Figure 2a), each animal was sedated using an anesthetic mixture of atropine (0.05 mg/kg) and ketamine (30 mg/kg), and was supported through mechanical ventilation. Anesthesia was maintained with isoflurane/O₂ (1–5%). For image acquisition, an 8-channel cardiac anterior array coil was placed on each pig. The heart rate and associated physiological signals were continuously monitored. The proposed MR imaging protocol presented in this paper included: a short-axis 2D CINE sequence for heart function evaluation, as well as a high-resolution 3D late gadolinium enhancement (LGE) for the identification and quantification of fibrosis. Amiodarone was injected in order to avoid arrhythmic events during the MR imaging study, which kept the heart rate stable and below 100 bpm. The heart rate stabilization improved image acquisition process and, consequently, the quality of reconstructed images.

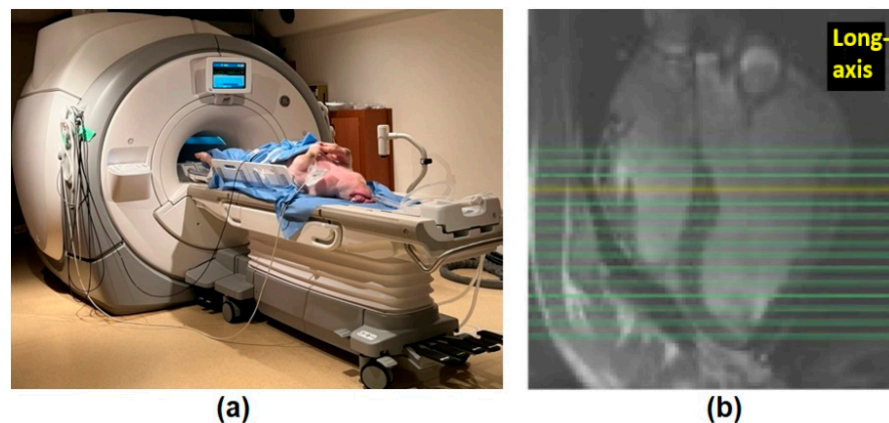


Figure 2. Example of a preclinical MR imaging study: (a) experimental set-up with the pig on the table of the 3T MR scanner (prior to placing the animal inside the bore); and (b) long-axis image serving for the prescription of the short-axis Cine images.

As per the diagram previously presented in Figure 1, the MR images were acquired at the following time points: (a) at baseline healthy state (pre-DOX injections) in both groups; (b) at one week after the completion of DOX injections in all four animals; (c) at five weeks post-DOX injections in Group 1 (i.e., in pig #1 and pig #2, respectively), and (d) at nine weeks post-DOX injections in Group 2 (i.e., in pig #3 and pig #4, respectively).

For the assessment of cardiac function, we utilized a steady-state free precession (SSFP) sequence in Cine mode, with the following MR parameters: 16–20 short-axis slices

to cover the entirety of the heart (prescribed on longitudinal-axis images, as in Figure 2b), 8 views/segment, 20 cardiac phases/slice, repetition time TR = 4.2 ms, echo time TE = 1.8 ms, flip angle = 45°, matrix size = 224 × 160, in-plane resolution of 1 mm × 1 mm, and slice thickness = 5 mm (with no gap between slices). All Cinematic images were acquired using ECG-gating and breath holds.

Contrast-enhanced imaging was performed by employing a free-breathing 3D late gadolinium enhancement (LGE) method, approximately 5–6 min after injecting a bolus of gadolinium-based contrast agent Gd-DTPA (0.2 mmol/kg, Magnevist, Bayer Healthcare Pharmaceuticals, Berlin, Germany). The 3D LGE method with isotropic voxels size was based on a 3D inversion recovery fast gradient echo (IR-FGRE) sequence with fat suppression and respiratory navigation (initial inversion time TI = 300 ms, repetition and echo times TR/TE = 3.5/1.5 ms, bandwidth BW = 100 kHz, flip angle = 15°, and an isotropic spatial resolution of 1.4 mm × 1.4 mm × 1.4 mm), similarly to the method we previously used in preclinical MR imaging studies to evaluate chronic infarct scars [16].

2.3. MR Image Analysis

First, the Cine images were analyzed with the CVI42 software (Circle Cardiovascular Imaging, Calgary) [17], to assess left ventricular function. The endocardial and epicardial contours were semi-automatically delineated, and then corrected by a clinical expert (cardiologist I.R.). Using these contours, we derived the end-systolic and end-diastolic volumes (ESV and EDV, respectively). The ejection fraction (EF) functional parameter was then calculated with the well-known formula: $EF(\%) = (EDV - ESV)/EDV$, for each dataset (i.e., each time-point), allowing us to observe the longitudinal changes over the weeks following the completion post-DOX delivery.

Second, the LGE images were analyzed using in-house custom scripts written in Matlab (Mathworks, Torrance, CA, USA), according to the image analysis pipeline illustrated in Figure 3. Briefly, for each raw MR image, we first performed manual endocardial and epicardial contouring of the LV. A region of interest (ROI) was selected from the remote myocardium on the posterior side. Subsequently, pixel-wise maps of signal intensity within the segmented LV were used as input to an algorithm able to differentiate healthy myocardium vs. fibrotic pixels based on a simple signal intensity thresholding method.

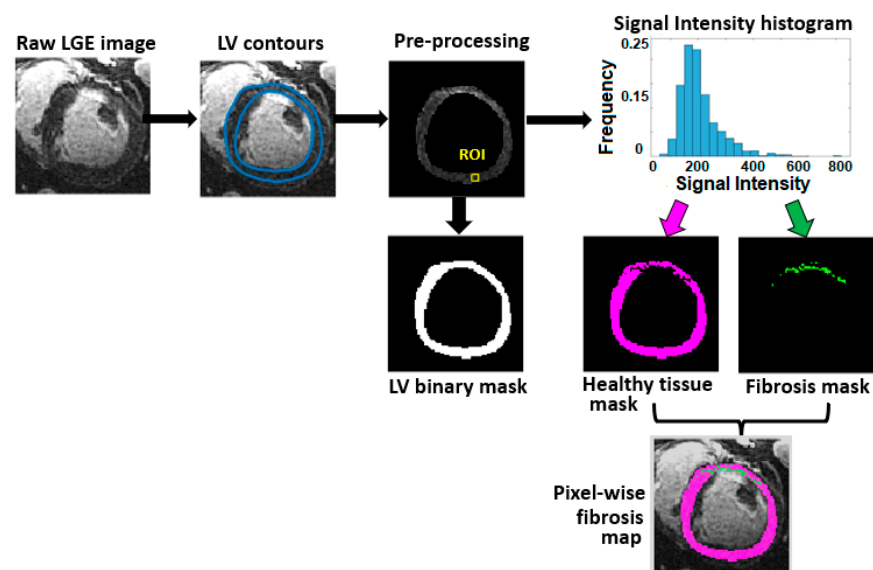


Figure 3. Diagrammatic illustration of the analysis pipeline used to generate pixel-wise fibrosis maps from high resolution LGE images (see text for more details). Note: fibrosis pixels are represented in green and healthy myocardium pixels in magenta.

Specifically, in order to cluster the pixels into the two distinct regions (i.e., fibrosis and healthy tissue), we used a 5 standard deviation (SD) threshold for signal intensity, which is

clinically accepted for fibrosis assessment [18]. Moreover, the LV binary masks were used to calculate the LV volume for each heart. At each time-point, for each heart, the density of fibrosis (%) was calculated as the ratio between the fibrosis volume (derived from the total number of segmented fibrosis voxels in each LV) and the LV volume.

2.4. Electrophysiology Studies (Mapping and Arrhythmia Test)

The day following the imaging studies at 9 weeks post-DOX, catheter-based electro-anatomic mapping (EAM) and an arrhythmia inducibility test were performed in pigs #3 and #4, respectively. An additional EAM study and arrhythmia test was performed in a healthy (control) pig. All animals were intubated and sedated, and anesthesia was maintained throughout these EAM procedures using the same combination of medications as those administered prior to the MR imaging scans. However, amiodarone was not administered, since one objectives of the EP study was to evaluate arrhythmia inducibility.

All three interventional electrophysiology EP studies were carried out under X-ray guidance, using a C-arm Toshiba INFINIX VF-I/SP-S (Figure 4a). Catheter-based EAM of the left ventricular (LV) endocardial surface was performed in these animals by employing a conventional CARTO3 electrophysiology system (Biosense Webster Inc, Diamond Bar, CA, USA). For the endocardial mapping procedures, we used a PentaRay[®] catheter (Biosense Webster Inc., Irvine, CA, USA) inserted into the LV cavity, via femoral access.

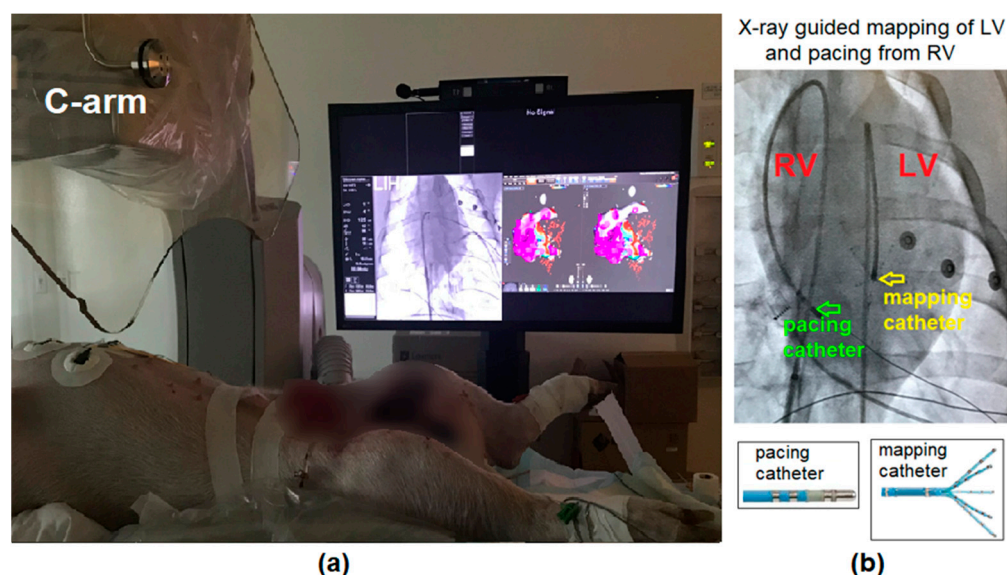


Figure 4. (a) Experimental set-up of the EP study (electro-anatomic mapping and arrhythmia study) shown during the intervention in pig #3, at week 9 following the completion of DOX injections; and (b) X-ray image of the mapping and pacing catheters inside the heart during the EP study.

The EAMs were primarily acquired for the purpose of constructing detailed bipolar voltage maps (i.e., more than one thousand points per map, in sinus rhythm and under pacing conditions). The bipolar voltages characterized by low amplitude values (0.1–1.5 mV) were attributed to patches of fibrotic tissue, whereas the areas with an amplitude voltage > 1.5 mV were considered normal, in accordance with the clinical threshold typically used to define scarred tissue [19]. The low bipolar voltage areas were qualitatively compared to those defined by LGE using ADAS 3D software, version 2.11.1-beta.2 (www.adas3D.com, accessed on 31 October 2022). Several representative points that had low voltage values (denoting fibrosis) were selected for a qualitative evaluation of the QRS and QRS-T intervals.

For the arrhythmia inducibility test, we inserted an SF Thermocool catheter (Biosense Webster Inc., Irvine, CA, USA) into the right ventricle (RV) and performed rapid pacing of the heart. Figure 4b shows an exemplary X-ray image of the heart during the EP study (in pig #3), with the pacing catheter inside the RV and the mapping catheter (with 5 prongs

and multiple sensors on each prong) inside the LV. The external ECGs placed onto the animal torso for reference, are also visible.

2.5. Histology

Except for pigs #3 and #4 (in which death was caused by VF), the other three animals were euthanized as per the approved protocol. All five hearts were carefully explanted, then fixed and preserved in formaldehyde solution for at least 1 week in order to ensure a uniform preservation of tissue. Tissue samples were collected from each heart and select cross-sections (i.e., slices cut at 4 mm thickness) corresponding to short-axis MR images (as guided by anatomical landmarks) were cut at 4 μm thickness. These were mounted on large glass slides and stained with collagen-specific Mason Trichrome stain to visualize the deposition of collagenous/reactive fibrosis. Following staining, the slides were digitally scanned using a special TissueScope (Huron Technologies, St. Jacobs, ON, Canada) that accommodates large pathology slides. These digital images were visualized using Aperio ImageScope [20], an open-source software specifically designed for pathological evaluation of digital images.

2.6. Statistical Analysis

Since this is a methodological protocol paper with the animal model being tested only in a small pilot study, the study was not powered statistically. Therefore, we focused on qualitative analyses and highlighting the longitudinal evolution of individual parameters (EF and fibrosis density) per animal.

3. Results

3.1. Longitudinal Assessment of LV Function from Cine Images

Figure 5a shows examples of LV contours at end diastole (ED) and end systolic (ED) phases in a short-axis cine slice, at different time-points (i.e., pre-DOX, week 1 post-DOX, and week 9 post DOX), taken from pig #3. For qualitative comparison, the slices were selected to be at the approximate same level using anatomical markers (e.g., papillary muscle as well as geometrical shape/features of the left ventricular endocardial wall), taken into consideration that the hearts of these juvenile swine had slightly grown in size between the time points of MRI scans (starting from the first pre-DOX scan and onward).

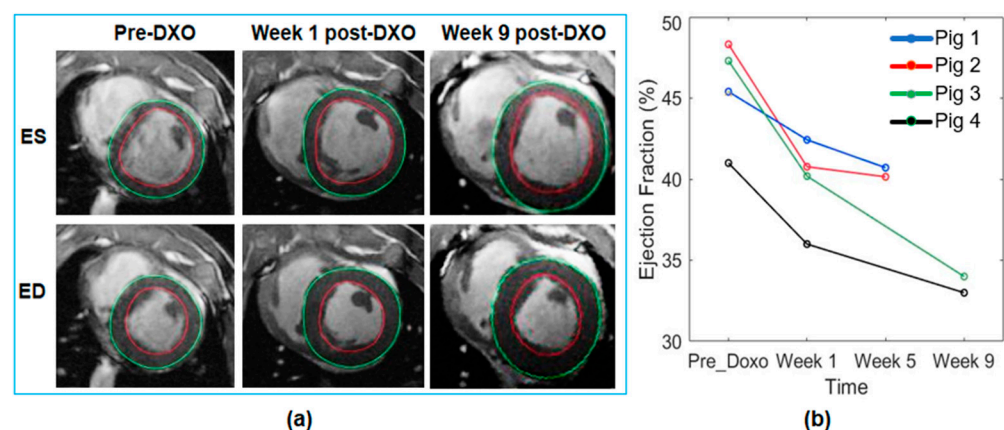


Figure 5. Characterization of the LV function through analysis of Cine MR images: (a) example of short-axis slice at mid-heart level, representing the end-systole and end-diastole phases during the cardiac cycle at different time points pre-DOX and post-DOX in pig #3 (ED = end-diastole, ES = end-systole); and (b) temporal evolution of the individual EF (%) parameter for each animal.

All animals had normal cardiac function prior to DOX injections, with EF values ranging from 41% to 48%. Overall, the EF values gradually decreased over time in each pig post-DOX. We observed that initially, all EF values clearly decreased by week 1 post-DOX. At week 5 post-DOX, the EF values for both pig #1 and pig #2 decreased, but not below

40%, whereas at week 9 post-DOX, the EF values decreased to less than 35% for both pig #3 and pig #4. The temporal evolution of the functional EF parameter in each animal is plotted in Figure 5b, where the steady DOX-induced decline in cardiac function is obvious on an individual heart basis.

3.2. Longitudinal Assessment of MRI-Defined Fibrosis Density

Figure 6 illustrates exemplary results from the segmentation of LGE images in pig #1 and pig #3 using the 5SD threshold to detect fibrosis, at different post-DOX time-points.

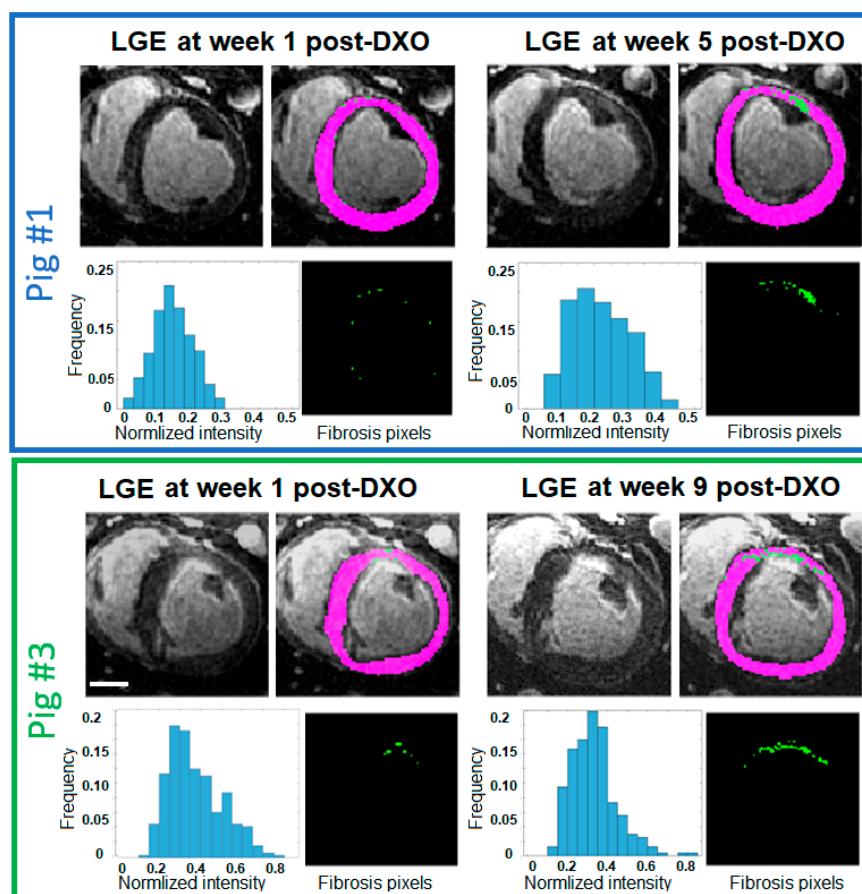


Figure 6. Representative results obtained by segmenting LGE images to distinguish fibrotic pixels (in green) from normal myocardium pixels (in magenta). For the green masks segmented in the MR slices presented, for pig #1, there are 11 fibrosis pixels out of 1003 total pixels of the LV at 1 week post-DOX, and 43 pixels out of 1092 pixels of LV at 5 weeks post-DOX. For pig #3, there are 11 pixels out of 905 LV pixels at 1-week post-DOX, and 65 pixels out of 939 LV pixels at week 9 post-DOX. White scalebar is 2 cm.

The LGE-defined pixels of fibrosis are depicted in green, whereas the healthy myocardium is depicted in magenta. The overall higher values of signal intensity in LV (as observed in the histograms) suggest an overall increase in fibrosis. We also observed that most pixels classified as ‘fibrosis’ (based on a higher signal intensity compared to the rest of myocardium in the LV), were scattered within the anterior territory and had a typical appearance of diffuse fibrosis in contrast-enhanced MR images.

The results from the estimation of fibrosis density from segmented LGE images are presented in Figure 7, along with representative histological images of collagen-sensitive Masson Trichrome stain. The qualitative increase in the deposition of reactive fibrosis post-DOX observed in the histopathological images was found to be in good agreement with the gradual increase in LGE-defined fibrosis. Figure 7a includes the temporal evolution of LGE-defined fibrosis density (%) post-DOX treatment, plotted individually for each animal.

Figure 7b demonstrates a gradual deposition of reactive interstitial fibrosis (caused by an increased extracellular matrix deposition) using samples selected from the healthy (control) animal, pig #1, and from pig #3. Typically, collagenous tissue stains blue-green, whereas healthy tissue stains dark red. The nuclei stain black, appearing pycnotic (i.e., smaller and condensed) or completely disappearing in the cells within more extensive fibrotic patches. In addition, we also noticed that by week 5 and week 9 post-DOX, respectively, there were no visible areas with edematous tissue or accumulated fluid.

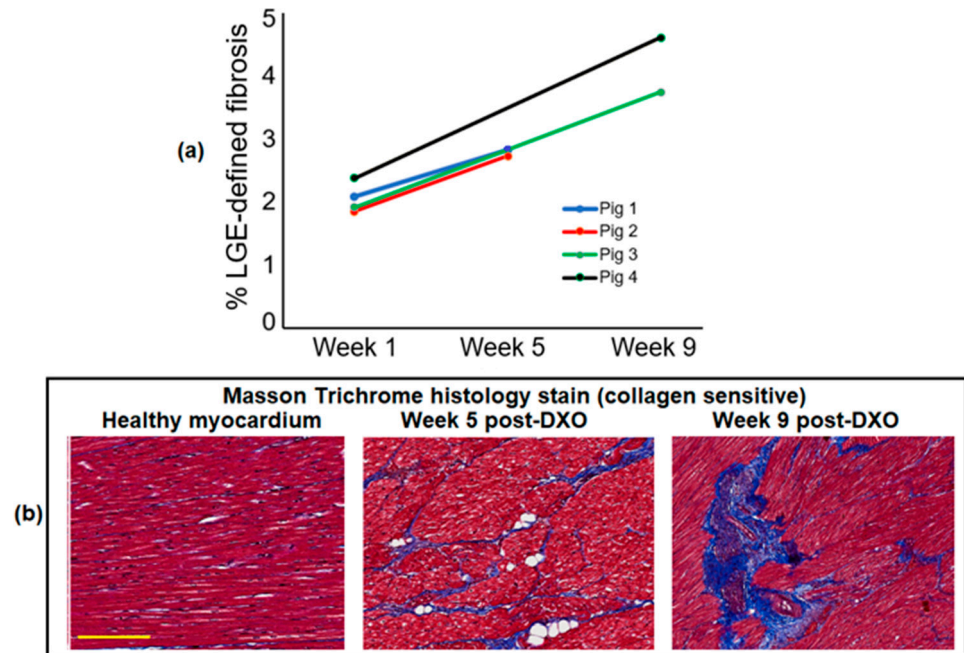


Figure 7. Results from the LGE-based evaluation of fibrosis density (calculated relative to the LV volume) for each animal, along with selected histopathological images denoting increased collagen deposition: (a) temporal evolution of LGE-defined fibrosis density from LGE images for each pig; (b) examples of Masson Trichrome stained samples from the control animal as well as from samples collected at 5 weeks and 9 weeks post-DOX, showing an increasing deposition of interstitial collagen and reactive fibrosis (in agreement with results obtained from MRI). The yellow scale-bar is 200 μm.

3.3. EP Studies (EAM Mapping and Arrhythmia Inducibility Tests)

Figure 8a–c illustrates examples of endocardial bipolar voltage maps, along with representative intracardiac electrograms (iEGMs), recorded following a retrograde aortic approach: (a) in the healthy control pig; (b) in pig #3; and (c) in pig #4, respectively. The healthy tissue (depicted in magenta) was defined by bipolar voltages with amplitude >1.5 mV, whereas small patches of fibrosis (depicted in dark red and green) had bipolar voltages <1.5 mV, as is typical for the clinical threshold that defines unexcitable fibrotic scars.

Figure 8d,e illustrates the 3D segmented LGE images for pig #3 and pig #4 after registration with endocardial bipolar voltage maps from CARTO3. The LGE-CARTO3 registration was performed in ADAS 3D, using a rigid landmark-based approach with 8 fiducial markers and the endocardial surface (i.e., taking a 5% layer closest to the surface) of the myocardium defined from the 3D LGE images.

Overall, both methods (LGE and CARTO3) revealed small patches of fibrosis scattered on the endocardial surface, especially on the anterior side of these two hearts. However, a precise geometrical correspondence between the locations of patches in the LGE shell vs. those in bipolar voltages cannot be found. This is due to the different spatial resolutions used, with the voxels in LGE images being of small size (1.4 mm × 1.4 mm × 1.4 mm) with the recorded bipolar voltage points several mm apart. The resulting slightly larger fibrotic patches defined by CARTO3 (compared to those seen in the LGE endocardial shells), were

likely due to the surface interpolation of the recording points. Furthermore, it is possible that there were a few very small fibrotic points that were missed by the contact catheter, but these likely appeared in the LGE-defined endocardial shell.

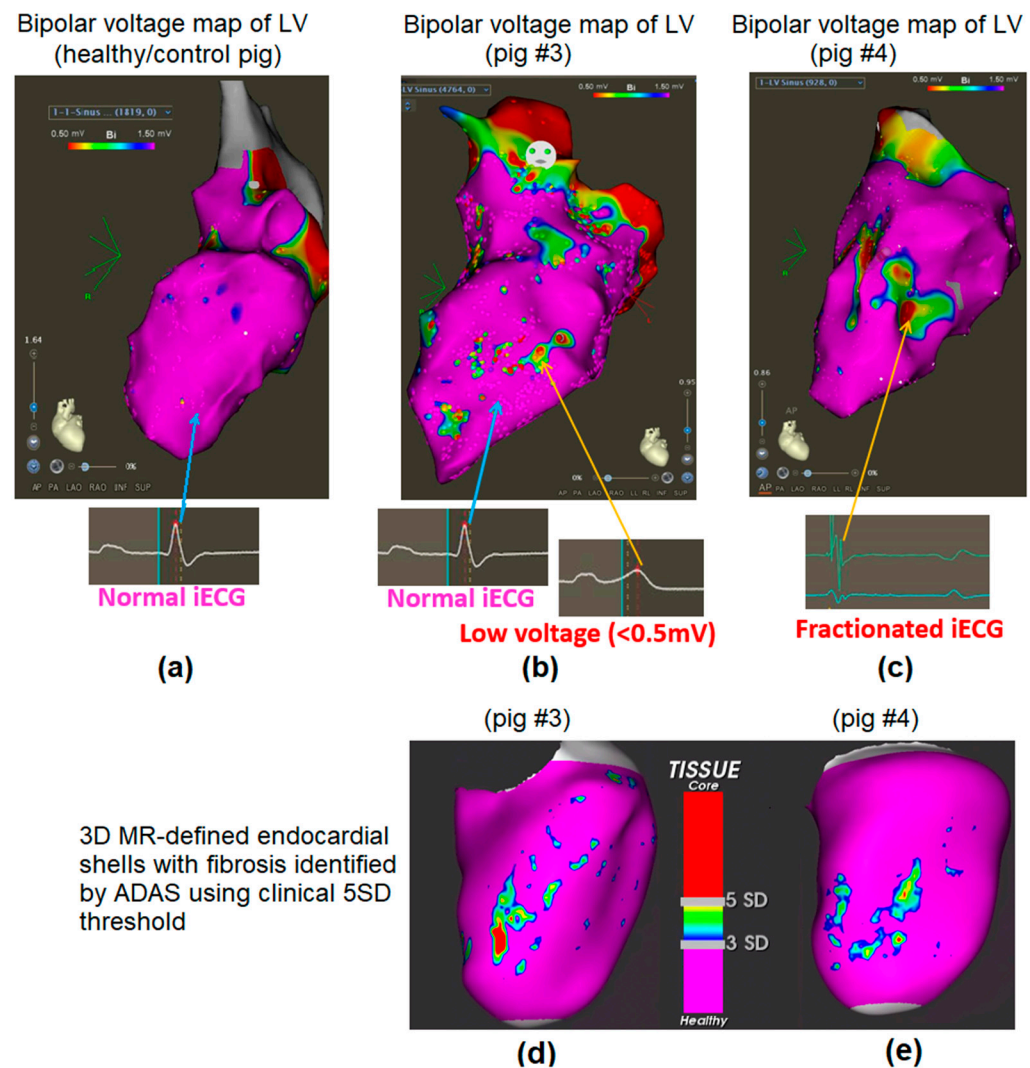
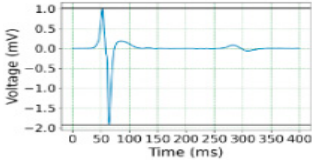
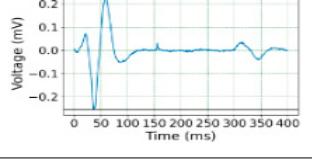
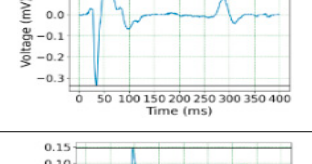
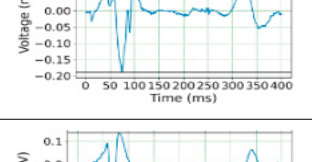
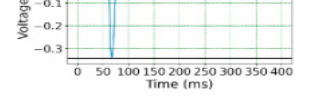


Figure 8. Examples of endocardial bipolar voltage maps, along with representative iEGM waves are presented for the healthy pig (a), pig #3 (b) and pig #4 (c). The location of low bipolar voltages in (b,c) agreed well with the with the corresponding location of LGE-defined fibrosis using the ADAS 3D software, as illustrated for pig #3 (d) and pig #4 (e). In both endocardial maps (i.e., from CARTO3 and segmented LGE shells), the fibrotic areas are indicated by red-green, while the healthy tissue is in magenta.

Examples of wave analysis for QRS and QRS-T intervals for a few selected fibrosis points are included in Table 1. Note that the recorded iEGM waves were evaluated for reproducible morphological appearance within three consecutive QRS heart beats prior to the acquisition window, using the 12-lead ECGs as reference. The QRS-T intervals were clearly prolonged for the points of low voltage compared to those in the healthy pig. In addition, the QRS intervals for these points were slightly longer in pig #4, but fluctuated in pig #3.

Table 1. QRS and QRS-T intervals and exemplary iEGM waves for points of low bipolar voltage (<0.5 mV) selected from pig #3 and pig #4, along with reference intervals from healthy pigs.

Animal ID	Intracardiac EGM Waves	Bipolar Voltage (mV)	QRS Interval (ms)	Q-T Interval (ms)
Healthy Ref.		3.00	56	290
Pig 4		0.29	65	338
Pig 4		0.48	59	338
Pig 4		0.33	63	351
Pig 4		0.37	61	357
Pig 3		0.5	47	293
Pig 3		0.34	47	306
Pig 3		0.48	56	307

Note that CARTO typically saves 2.5 s of recording prior to the moment a bipolar voltage is acquired to be projected on the anatomical shell. In Table 1, we presented the signal captured during the acquisition window, which was set before the QRS and T waves, within the time window of 400 ms during sinus rhythm. In evaluating iEGMs for reproducible morphological appearance in the regions of low voltage identified from registered segmented LGE and bipolar maps, we identified consistent morphological

appearance of low voltage intracardiac recordings at the fibrotic regions within 3 QRS beats of the projected bipolar voltage signal, suggesting acceptable reproducibility.

Figure 9 shows examples of recorded iEGMs and reference 12-lead ECGs in pig #3, during: sinus rhythm (650 ms R-R interval), pacing at 500 ms and induced ventricular fibrillation, VF. In both animals in Group 2 (i.e., pig #3 and pig #4) VF was induced via rapid pacing (<300 ms); however, it could not be induced in the healthy control animal, regardless of the pacing rate. These observations, corroborated by the recorded bipolar voltage maps and the MRI-derived fibrosis maps suggested that the small patches of diffuse fibrosis identified in histopathology images acted as small anatomical obstacles and perturbed the normal propagation of electrical waves through the heart. These scattered patches likely broke the propagating waves into smaller spiraling waves, and in conjunction with their corresponding prolonged QRS-T intervals, favored a chaotic electrical propagation specific to fast and lethal VF. Note that these two pigs were not defibrillated, as such a maneuver was out of the scope of this study.

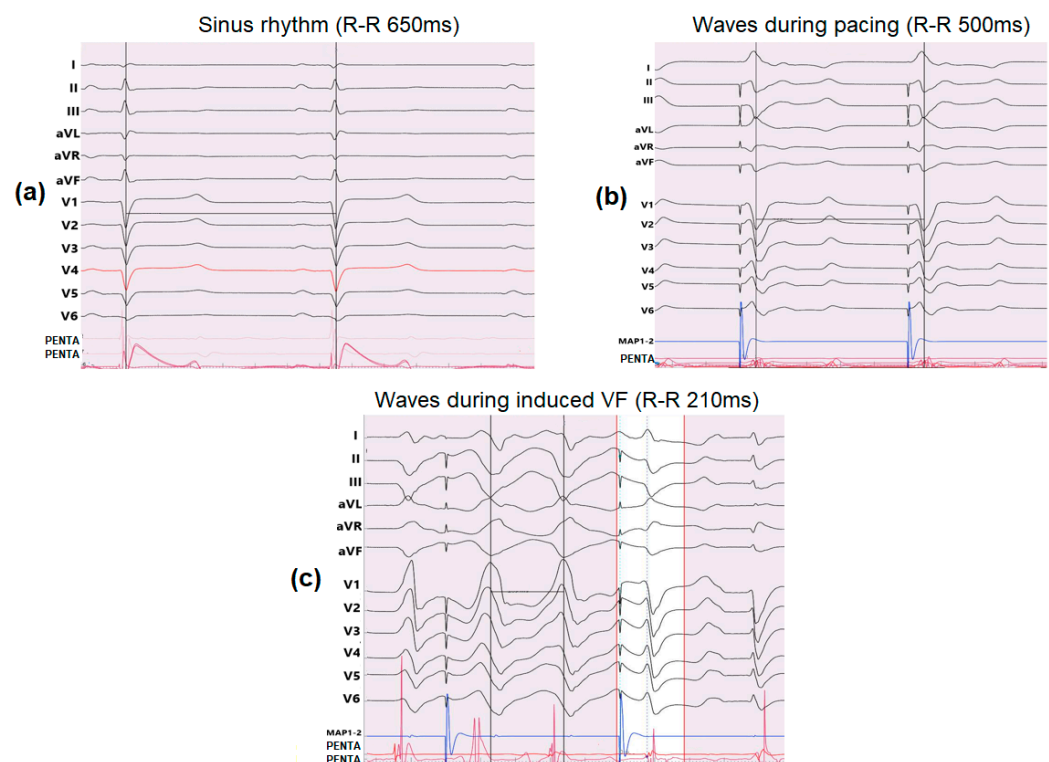


Figure 9. Examples of iEGMs and reference ECG waves in pig #3 at 9 weeks post-DOX, during: (a) sinus rhythm; (b) pacing from RV at 2 Hz resulting in a cardiac cycle length of 500 ms; and (c) induced ventricular fibrillation (VF) that resulted in a fast cycle length of 210 ms.

4. Discussion

Accurate identification of characteristics specific to reversible and irreversible myocardial remodeling post-chemotherapy could help clinicians to assess the long-term effects of DOX therapy and to predict the risk of sudden cardiac death associated with heart failure [21]. A major role in the identification of early cardiotoxic signs (weeks and months post-DOX) can be played by cardiac imaging. Among the various imaging methods nowadays available to characterize cardiac function [22] and structure [9,11], MR imaging may soon be the preferred technique for evaluating myocardial injury post-chemotherapy [23], owing to its robust imaging sequences and excellent tissue contrast.

In this work, we demonstrated the feasibility of a large animal (swine) model to explore functional and subtle structural cardiotoxic changes induced by DOX. As a first novel aspect of our protocol, in distinction to the catheter-based intracoronary delivery employed by other researchers in pig models [14,15], in our pilot study, we successfully used

non-invasive intravenous (i.v.) injections of DOX, similarly to the clinical chemotherapeutic approaches. Our histologically validated results clearly demonstrated that reactive fibrosis occurred as a side-effect of the DOX treatment within the first couple of months, following the completion of one 4-week cycle of treatment. The deposition of fibrosis appeared to lead to an irreversible ventricular mechanical dysfunction, although we acknowledge that a monitoring period longer than 9 weeks could better support this observation. With this respect, we suggest that future studies could replace the Yorkshire swine with Yucatan pigs, since the latter animals do not gain weight (in time) and therefore they could better fit in the relatively narrow bore of 3T MR scanners.

A second novel aspect is related to the identification of scattered pixels of fibrosis in the high-resolution 3D LGE images. Compared to clinical 2D MR scans that typically use 8–10 mm slice thickness, our 3D LGE method is superior in overcoming issues associated with partial volume effects, which are problematic particularly in the setting of diffuse fibrosis. Furthermore, our Cine and LGE MR imaging methods are both superior, in terms of spatial resolution, to those used in other preclinical DOX studies. For example, for functional imaging, our voxel size was $1\text{ mm} \times 1\text{ mm} \times 5\text{ mm} = 5\text{ mm}^3$ (which is four times smaller than the voxel size of $1.8\text{ mm} \times 1.8\text{ mm} \times 6\text{ mm} = 19.6\text{ mm}^3$ used by Galán-Arriola et al. in [15]). For the LGE method, we used a voxel size of $1.4\text{ mm} \times 1.4\text{ mm} \times 1.4\text{ mm} = 2.74\text{ mm}^3$, which is smaller compared to the $\sim 3.75\text{ mm}^3$ voxels used in [15]. The higher the spatial resolution is, the less significant the partial volume effects are; thus, we suggest that our MR imaging methods may provide more accurate functional parameters and structural information. Moreover, the authors of ref. [15] only presented raw LGE images, without specifically identifying the fibrotic pixels using clinically accepted algorithms as in our study.

Our free-breathing, high resolution 3D LGE method appears more adequate for pixel-wise quantitative analysis of collagen density than the 2D T1 mapping images acquired at 5 mm slice thickness [24]. However, LGE imaging is known to be sensitive to contrast injections, and the image analysis based on 5SD threshold is user-dependent (i.e., with respect to the selected ROIs), while T1 mapping techniques are more robust [25]. Given the important role of diffuse fibrosis in post-chemotherapy [26], our future work will focus on implementing a high-resolution 3D T1* mapping method. This method has the capability to distinguish dense collagenous fibrotic patches, as demonstrated in a previous study performed ex vivo in chronically infarcted porcine hearts [27], and has already been translated to preclinical in vivo free-breathing 3D imaging of infarct scars, using a 1.4 mm isotropic resolution [16]. Furthermore, in the imaging protocol, we plan to include T2-based methods to evaluate edema resorption, a reversible side-effect of DOX which we recently observed in [24] (in three animals). Lastly, with respect to cardiac functional assessment, the gradual decline in ejection fraction observed in the current work within the first 9 weeks post-DOX indicated an early sub-acute and sub-chronic occurrence of biomechanical dysfunction, in agreement with the swine study of cardiotoxicity that used intracoronary DOX injections [15]. We suggest that the collagen deposition has substantially contributed to the overall EF decline, and will likely have a critical role in the further evolution towards heart failure.

Regarding the third novel aspect, to the best of our knowledge, this is the first pre-clinical study to report X-ray guided electro-anatomical mapping of endocardial bipolar voltages in a large animal model post-chemotherapy, as most studies have focused only on longitudinal assessment of cardiac mechanical function. The recorded intracardiac iEGM signals, acquired with a catheter-based clinical systems, revealed small patches of fibrotic tissue with reduced bipolar voltage amplitude, which is typically seen clinically in scarred myocardium post-infarction. Our findings also suggest that early electrical remodeling takes place within the first couple of months post-DOX, with prolonged QRS-T intervals accompanying the low voltages in fibrotic areas. The small patches of dense collagenous fibrosis located within areas of abnormal iEGM waves' morphology likely created unexcitable obstacles in the electrical wave pathway, generating reentrant waves, spiral wave break, and chaotic electrical propagation. This eventually led to lethal ventricular

fibrillation during the rapid pacing procedure, similarly to the scar-related ventricular arrhythmias induced in post-infarction. Future work will include the monitoring of spontaneous arrhythmia episodes via MR-compatible implantable cardioverter defibrillators, in order to study the risk of lethal arrhythmia development post-chemotherapy.

We acknowledge that one study limitation is the small number of animals. However, in this work, we aimed to describe in detail the experimental protocol and qualitative results, using a minimum number of animals for tests and respecting the '3Rs principle' in animal research (i.e., replacement, reduction, and refinement). Nonetheless, we plan to expand the cohort in the future by including more animals, which will enable us to give statistical power to the study.

We envision that preclinical large animal models of cardiotoxicity will substantially help researchers better understand the mechanistic effects of cardiotoxicity. Such models can also provide a robust translational platform for testing new individual cardio-protective strategies or a synergistic combination of those [28,29]. These could slow the irreversible myocardial injury and associated dysfunction post-chemotherapy, and restrict further progression towards the heart failure stage. Our future work will also focus on testing 3D virtual models in order to predict the electro-mechanical function post-cardiotoxicity, integrating MRI-defined fibrosis areas and electrical remodeling information. Such *in silico* computer models can be exploited to virtually predict risk of arrhythmia and impaired mechanical contraction (including the EF index) [30] either for screening of drugs' cardiotoxicity [31] or to design more efficient therapeutic strategies, in conjunction with information provided by early imaging biomarkers and knowledge gained from animal models of cardiotoxicity [32].

5. Conclusions

Overall, this feasibility pilot study suggests that swine models of cardiotoxicity (based on *i.v.* DOX delivery) can be used for revealing key signs of functional and structural changes via non-invasive MRI, along with the risk of lethal arrhythmia in the sub-chronic phases following DOX injections. Our protocol can be further employed to test various cardioprotective strategies in order to minimize the myocardial injury post-DOX. Notably, MR imaging biomarkers may be able to help predict late cardiotoxic effects of therapy from the early reversible and irreversible alterations (i.e., fibrosis) of myocardial tissue. Thus, such image-based translational large animal models and protocols could play an important role in finding effective solutions to improve the delivery of cancer therapies (e.g., synergistic combinations of anti-cancer drugs with statins, mitigating their optimal combined dose and therapeutic plan), while considerably reducing the progression to heart failure, as well as the mortality and morbidity associated with it.

Author Contributions: Study design: P.L. and M.P.; preclinical animal model development: M.L. (Melissa Larsen) and J.B.; imaging and electrophysiology studies: T.E., M.L. (Melissa Larsen), J.B., P.L. and M.P.; data analysis and figures: P.L., T.E., M.N., M.L. (Mengyuan Li), I.R. and M.P.; draft writing, M.P.; final manuscript, P.L., T.E., M.N., M.L. (Melissa Larsen), J.B., M.L. (Mengyuan Li), I.R. and M.P.; funding secured by M.P. All authors have read and agreed to the published version of the manuscript.

Funding: This research was funded by Canadian Institutes of Health Research (CIHR), Project grant: PJT 153212 awarded to Principal Investigator Dr Mihaela Pop.

Institutional Review Board Statement: This study did not use sensitive data, patient information, or any other identity data. This animal study received ethics approvals.

Informed Consent Statement: This study did not require consent from patients or otherwise.

Data Availability Statement: This work in progress is focused on the development of a research protocol, with the associated methodology being described in detail for study reproducibility and the preclinical model being tested only in a small cohort of animals. The collection of more data (for statistical power) has not been completed; thus, the authors cannot make the current data available until after the full completion of the study.

Acknowledgments: The authors would like to thank Adebayo Adeeko for processing the explanted hearts and for staining the histology slides, Xiuling Qi for assistance with initial imaging scans (both from Sunnybrook Research Institute, Toronto, ON, Canada), and to Susan Camilleri (The Center for Phenogenomics, Toronto, ON, Canada) for help with histopathological interpretation of Masson Trichrome slides.

Conflicts of Interest: The authors declare no conflict of interest.

References

1. Kostakou, P.M.; Kouris, N.T.; Kostopoulos, V.S.; Damaskos, D.S.; Olympios, C.D. Cardio-oncology: A new and developing sector of research and therapy in the field of cardiology. *Heart Fail. Rev.* **2018**, *24*, 91–100. [CrossRef] [PubMed]
2. Von Hoff, D.D.; Rozenzweig, M.; Piccart, M. The cardiotoxicity of anticancer agents. *Semin. Oncol.* **1982**, *9*, 23–33. [PubMed]
3. Christiansen, S.; Autschbach, R. Doxorubicin in experimental and clinical heart failure. *European. J. Cardiothorac. Surg.* **2006**, *30*, 611–616. [CrossRef] [PubMed]
4. Podyacheva, E.Y.; Kushnareva, E.A.; Karpov, A.A.; Topopova, Y.G. Analysis of models of doxorubicin-induced cardiomyopathy in rats and mice: A modern view from the perspective of the pathophysiological and the clinician. *Front. Pharmacol.* **2021**, *12*, 670479. [CrossRef] [PubMed]
5. Angsutararux, P.; Luanpitpong, S.; Issaragrisil, S. Chemotherapy-induced cardiotoxicity: Overview of the roles of oxidative stress. *Oxid. Med. Cell Longev.* **2015**, 795602. [CrossRef] [PubMed]
6. Varga, Z.V.; Ferdinandy, P.; Liaudet, L.; Pacher, P. Drug-induced mitochondrial dysfunction and cardiotoxicity. *Am. J. Physiol. Heart Circ. Physiol.* **2015**, *309*, H1453–H1467. [CrossRef] [PubMed]
7. Herrmann, J. Adverse cardiac effects of cancer therapies: Cardiotoxicity and arrhythmia. *Nat. Rev. Cardiol.* **2020**, *17*, 474–502. [CrossRef]
8. Kang, Y.; Scherrer-Crosbie, M. Echocardiography Imaging of Cardiotoxicity. *Cardiol. Clin.* **2019**, *37*, 419–427. [CrossRef]
9. Safaei, A.M.; Kamangar, T.M.; Asadian, S.; Rezaeian, N.; Esmati, E.; Kolahdouzan, K.; Hosseini, L.; Lashkari, M.; Jafari, F.; Hashemi, F.A. Detection of the early Cardiotoxic effects of doxorubicin-containing chemotherapy regimens in patients with breast cancer through novel cardiac magnetic resonance imaging: A short-term follow-up. *J. Clin. Imaging Sci.* **2021**, *11*, 33. [CrossRef]
10. Roifman, I.; Ghugre, N.; Zia, M.; Zavodni, A.; Pop, M.; Connelly, K.; Wright, G. Assessment of the longitudinal changes in infarct heterogeneity. *BMC-Cardiovasc. Disord.* **2016**, *16*, 198. [CrossRef]
11. Tahir, E.; Azar, M.; Shihada, S.; Seiffert, K.; Goy, Y.; Beitzel-Heineke, A.; Molwitz, I.; Muellerleile, K.; Stehning, C.; Schön, G.; et al. Myocardial injury detected by T1 and T2 mapping on CMR predicts subsequent cancer therapy-related cardiac dysfunction in patients with breast cancer treated by epirubicin-based chemotherapy or left-sided RT. *Eur. Radiol.* **2022**, *32*, 1853–1865. [CrossRef] [PubMed]
12. Zeiss, C.J.; Gatti, D.M.; Toro-Salazar, O.; Davis, C.; Lutz, C.M.; Spinale, F.; Stearns, T.; Furtado, M.B.; Churchill, G.A. Doxorubicin-induced cardiotoxicity in collaborative cross (CC) mice recapitulates individual cardiotoxicity in humans. *G3 Genes | Genomes | Genet.* **2019**, *9*, 2637–2646. [CrossRef] [PubMed]
13. Hong, Y.J.; Park, H.S.; Park, J.K.; Han, K.; Park, C.H.; Kim, T.K.; Yoo, S.J.; Lee, J.Y.; Kim, P.K.; Hur, J.; et al. Early detection and serial monitoring of anthracycline-induced cardiotoxicity using T1-mapping cardiac magnetic resonance imaging: Animal study. *Sci. Rep.* **2017**, *7*, 2663. [CrossRef]
14. Balosetti, C.; Curnier, D.; Heon, H.; Dahdah, N.; Cheriet, F.; Friedrich, M.; Perie, D. Early detection of doxorubicin induced cardiotoxicity in the swine by cardiac MRI. *Can. J. Cardiol.* **2016**, *32*, S300. [CrossRef]
15. Galán-Arriola, C.; Lobo, M.; Vélchez-Tschischke, J.P.; López, G.J.; de Molina-Iracheta, A.; Pérez-Martínez, C.; Agüero, J.; Fernández-Jiménez, R.; Martín-García, A.; Oliver, E.; et al. Serial magnetic resonance imaging to identify early stages of anthracycline-induced cardiotoxicity. *J. Am. Coll. Cardiol.* **2019**, *73*, 779–791. [CrossRef] [PubMed]
16. Zhang, L.; Lai, P.; Pop, M.; Wright, G.A. Accelerated multicontrast volumetric imaging with isotropic resolution for improved peri-infarct characterization using parallel imaging, low-rank and spatially varying edge-preserving sparse modeling. *Magn. Reson.* **2018**, *79*, 3018–3031. [CrossRef]
17. Available online: <https://www.circlecvi.com/> (accessed on 1 April 2021).
18. Rashed, K.; Pranav, B.; Piet, C.; Housden, R.J.; Zhong, C.; Zahr, K.; Hyon-Mok, S.; Laura, R.; Sergio, V.; Xènia, V.; et al. Evaluation of state-of-the-art segmentation algorithms for left ventricle infarct from late Gadolinium enhancement MR images. *Med. Image Anal.* **2016**, *30*, 95–107.
19. Oduneye, S.O.; Pop, M.; Biswas, L.; Ghate, S.; Flor, R.; Ramanan, V.; Barry, J.; Celik, H.; Crystal, E.; Wright, G.A. Postinfarction ventricular tachycardia substrate characterization: A comparison between late enhancement magnetic resonance imaging and voltage mapping using an MR-guided electrophysiology system. *IEEE Trans. Biomed. Eng.* **2013**, *60*, 2442–2449. [CrossRef]
20. Available online: <https://aperio-imagescope.software.informer.com/> (accessed on 1 March 2021).
21. Steinherz, L.J.; Steinherz, P.G.; Tan, C.T.; Heller, G.; Murphy, M.L. Cardiac toxicity 4 to 20 years after completing anthracycline therapy. *JAMA* **1991**, *266*, 1672–1677. [CrossRef]
22. Panis, V.; Donal, E. Imaging techniques for cardiac function. *Appl. Sci.* **2021**, *11*, 10549. [CrossRef]

23. Wei, X.; Lin, L.; Zhang, G.; Zhou, X. Cardiovascular magnetic resonance imaging in the early detection of cardiotoxicity induced by cancer therapies. *Diagnostics* **2022**, *12*, 1846. [[CrossRef](#)] [[PubMed](#)]
24. Lin, P.; Escartin, T.; Ng, M.; Li, M.; Larsen, M.; Barry, J.; Roifman, I.; Pop, M. Novel imaging biomarkers to evaluate heart dysfunction post-chemotherapy: A preclinical MRI feasibility study. In *Lecture Notes in Computer Science*; Springer: Berlin/Heidelberg, Germany, 2022; Volume 13131, pp. 29–37.
25. Jordan, J.H.; Vasu, S.; Morgan, T.M.; D’Agostino, R.B., Jr.; Meléndez, G.C.; Hamilton, C.A.; Arai, A.E.; Liu, S.; Liu, C.Y.; Lima, J.A.; et al. Anthracycline-associated T1 mapping characteristics are elevated independent of the presence of cardiovascular comorbidities in cancer survivors. *Circ. Cardiovasc. Imag* **2016**, *9*, e004325. [[CrossRef](#)] [[PubMed](#)]
26. Meléndez, G.C.; Gregory Hundley, W. Is myocardial fibrosis a new frontier for discovery in cardiotoxicity related to the administration of anthracyclines? *Circul. Cardiovas. Imag* **2016**, *9*, 12. [[CrossRef](#)] [[PubMed](#)]
27. Pop, M.; Ramanan, V.; Yang, F.; Zhang, L.; Newbigging, S.; Ghugre, N.R.; Wright, G.A. High-resolution 3-D T1*-mapping and quantitative image analysis of gray zone in chronic fibrosis. *IEEE Trans. Biomed. Eng.* **2014**, *61*, 2930–2938. [[CrossRef](#)] [[PubMed](#)]
28. Octavia, Y.; Tocchetti, C.G.; Gabrielson, K.L.; Janssens, S.; Crijns, H.J.; Moens, A.L. Doxorubicin-induced cardiomyopathy: From molecular mechanisms to therapeutic strategies. *J. Mol. Cell. Cardiol.* **2012**, *52*, 1213–1225. [[CrossRef](#)] [[PubMed](#)]
29. Dragojevic, S.; Ryu, J.S.; Hall, M.E.; Raucher, D. Targeted drug delivery biopolymers effectively inhibit breast tumor growth and prevent doxorubicin-induced cardiotoxicity. *Molecules* **2022**, *27*, 3371. [[CrossRef](#)]
30. Marchesseau, S.; Delingette, H.; Sermesant, M.; Ayache, N. Fast parameter calibration of a cardiac electromechanical model from medical images based on the unscented transform. *Biomech. Model Mechanobiol.* **2013**, *12*, 815–831. [[CrossRef](#)]
31. Yuan, Y.; Bai, X.; Luo, C.; Wang, K.; Zhang, H. The virtual heart as a platform for screening drug cardiotoxicity. *Br. J. Pharmacol.* **2015**, *172*, 5531–5547. [[CrossRef](#)]
32. Park, C.J.; Brank, M.E.; Vasu, S.; Melendez, G.C. The Role of Cardiac MRI in Animal Models of Cardiotoxicity: Hopes and Challenges. *J. Cardiovasc. Transl. Res.* **2020**, *13*, 367–376. [[CrossRef](#)]